Supporting Information

for

Weberite Na$_2$MM'F$_7$ (M, M' = Redox-Active Metal) as Promising Fluoride-Based Sodium-Ion Battery Cathodes

Tenglong Lu[1,2], Sheng Meng[1,2,3]*, Miao Liu[1,3,4]*

[1]*Beijing National Laboratory for Condensed Matter Physics, Institute of Physics, Chinese Academy of Sciences, Beijing 100190, China*
[2]*School of Physical Sciences, University of Chinese Academy of Sciences, Beijing 100190, China*
[3]*Songshan Lake Materials Laboratory, Dongguan, Guangdong 523808, China*
[4]*Center of Materials Science and Optoelectronics Engineering, University of Chinese Academy of Sciences, Beijing 100049, China*

Corresponding author: smeng@iphy.ac.cn, mliu@iphy.ac.cn

(I) Polymorphism of weberite-type sodium metal fluorides
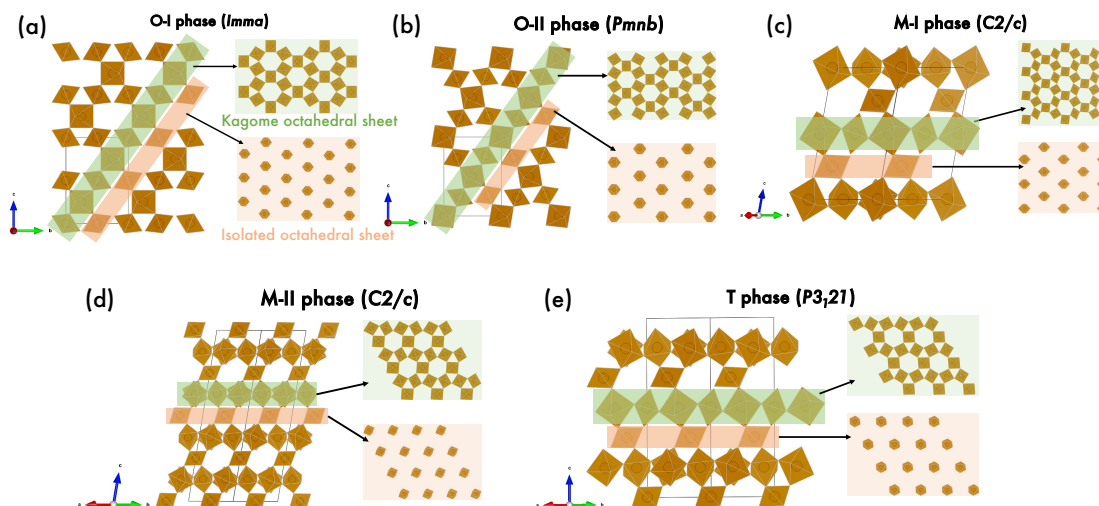
Figure S1. Topological analysis of the structural frameworks of the five polymorphs of weberite Na$_2$Fe$_2$F$_7$. Structural frameworks of (a) O-I phase, (b) O-II phase, (c) M-I phase, (d) M-II phase, and (e) T phase. The Kagome octahedral sheet and isolated octahedral sheet are labeled by green and pink boxes, respectively.
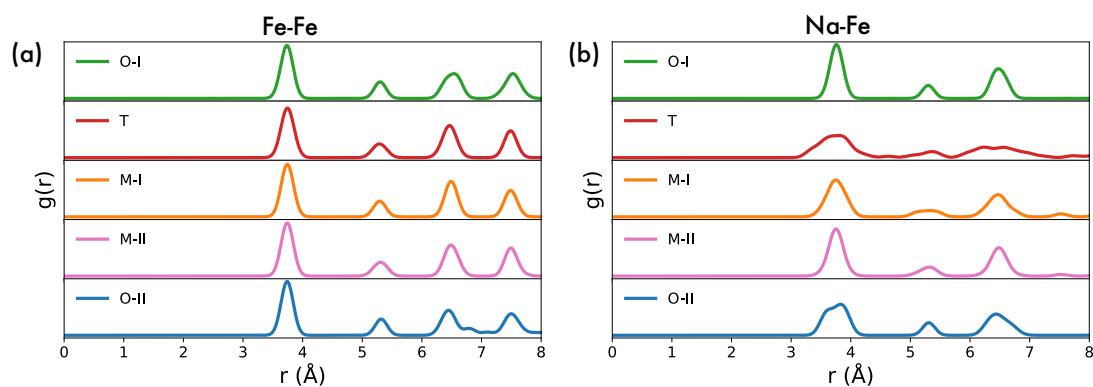
Figure S2. (a) Fe-Fe and (b) Na-Fe radial distribution function, *g(r)*, for the five polymorphs of weberite Na$_2$Fe$_2$F$_7$.

Table S1. Thermodynamic properties among 33 metal pairs for all five polymorphs of weberite compounds.

Metal pair	E_{hull} (meV)					Standard deviation (meV)
	O-I	O-II	M-I	M-II	T	
Ti-Ti	56.48	55.57	57.08	60.81	58.05	1.797
Ti-V	40.21	45.15	42.09	41.18	40.14	1.845
Ti-Ni	131.77	127.67	129.21	124.65	129.73	2.372
V-Ti	32.56	30.63	30.97	30.95	32.49	0.831
V-V	2.18	0.62	0.00	0.49	0.62	0.738
V-Cr	4.27	3.16	2.00	2.12	2.05	0.884
V-Ni	16.77	16.64	18.80	15.58	19.77	1.535
Cr-V	18.66	8.40	6.38	11.29	12.26	4.186
Cr-Cr	5.78	1.44	0.00	4.12	2.76	2.016
Cr-Mn	10.27	10.34	13.90	10.35	17.51	2.876
Cr-Fe	0.00	0.50	8.74	4.63	6.90	3.448
Cr-Ni	22.13	22.71	24.60	20.96	24.21	1.341
Cr-Cu	10.15	10.13	9.12	9.23	14.27	1.897
Mn-Ti	46.38	43.24	43.78	43.90	43.46	1.139
Mn-V	20.67	18.49	14.83	11.84	13.68	3.225
Mn-Cr	8.17	6.21	4.07	5.37	4.21	1.503
Mn-Mn	23.60	23.25	23.61	22.28	20.36	1.228
Mn-Fe	19.91	16.23	14.31	15.94	14.86	1.960
Mn-Ni	9.79	10.54	11.77	12.16	13.59	1.319
Fe-Ti	85.89	84.50	84.03	85.75	90.44	2.274
Fe-V	7.11	2.65	3.22	5.95	5.42	1.681
Fe-Cr	6.91	3.19	3.35	4.51	5.44	1.382
Fe-Fe	5.94	4.15	1.15	2.01	0.00	2.13
Fe-Ni	20.91	22.07	24.76	20.70	29.26	3.205
Fe-Cu	10.92	11.72	11.26	9.73	15.36	1.897
Ni-Ti	103.98	103.87	106.65	104.42	108.03	1.663
Ni-Cr	0.27	0.31	1.99	0.00	3.69	1.408
Ni-Mn	2.47	1.57	0.00	1.05	1.14	0.802
Ni-Fe	0.88	0.00	2.19	0.77	3.98	1.397
Ni-Ni	2.83	0.00	7.99	0.513	10.91	4.297
Cu-Cr	5.74	0.00	2.02	6.21	5.72	2.483
Cu-Fe	7.30	1.49	3.89	8.30	12.46	3.771
Cu-Cu	3.90	7.87	11.02	0.00	2.55	3.919

(II) Detailed Crystal Structure Information for T-Na$_2$MM'F$_7$ Compound

Crystal structure: Trigonal

Space group: $P3_121$ (152)

Lattice parameters: a = b = 7.3774 Å, c = 18.2288 Å

Volume: 859.2 Å^3

Table S2. Detailed structural information of T-Na$_2$MM'F$_7$ compound.[1, 2]

Atom	Wyckoff position	x	y	z	Occupancy
M'1	3a	0.337	0	0.33333	1
M'2	3b	0.337	0	0.83333	1
M	6c	0.480	0.842	0.1688	1
Na1	6c	0.523	0.849	0.6653	1
Na2	6c	0.949	0.186	0.3357	0.5
Na3	6c	0.902	0.169	0.8626	0.5
F1	6c	0.754	0.203	0.601	1
F2	6c	0.798	0.965	0.9487	1
F3	6c	0.566	0.413	0.0544	1
F4	6c	0.831	0.452	0.187	1
F5	6c	0.048	0.334	0.2729	1
F6	6c	0.224	0.230	0.1460	1
F7	6c	0.066	0.444	0.8546	1

(III) Evaluation of thermal stability

Oxygen release is one of the biggest safety concerns for oxide cathode materials, which can easily combust flammable organic electrolytes and eventually lead to fire. Given the even more violent exothermic processes that may occur in fluoride chemistry, this gas-releasing issue should also be treated with caution in fluoride cathodes. In this work, we analyzed the thermal safety of fluoride cathode materials by calculating the critical fluorine chemical potential (μ_{F_2}) at which the cathode begins to evolve fluorine gas. This methodology was modified from a previous work which investigated the thermal stability of LiMnPO4 and LiFePO4,[3, 4] and was described in detail below.

In an open system concerning fluorine, alterations in phase equilibria are predominantly due to reactions that involve the uptake or release of fluorine gas. The entropy of fluorine gas primarily dominates the reaction entropy in such reactions, with changes in fluorine chemical potential largely capturing the impact of temperature. The effect of temperature and partial pressure is mostly captured by changes in the fluorine chemical potential, as follows:

$$\mu_{F_2}(T, p_{F_2}) = \mu_{F_2}(T, p_0) + kTln\frac{p_{F_2}}{p_0}$$
$$= E_{F_2} + kT - TS_{F_2}^{T,p_0} + kTln\frac{p_{F_2}}{p_0} \qquad (S1)$$

where p_{F_2} is the fluorine partial pressure, p_0 is a reference fluorine partial pressure, $S_{F_2}^{T,p_0}$ is the fluorine entropy, E_{F_2} is the fluorine internal energy, and k is Boltzmann's constant. We set the reference fluorine chemical potential to be zero at 298 K and 1 atm. For fluorine gas, its experimental entropy data (at 0.1 MPa) under temperatures were obtained from NIST-JANAF thermochemical table.[5]

For each compound, we constructed a grand potential phase diagram at constant μ_{F_2} in the corresponding chemical space. Through evolving the phase diagram under different μ_{F_2}, the critical chemical potential at which the compound begins to release fluorine gas can be determined. Further, the gas-releasing temperature can be calculated

through Eq. S1. Note that given the differences between the simulated and real environments, no expectation should be taken of the accuracy of the quantitative value of the gas-releasing temperature. Nonetheless, our theoretical predictions can still provide insights on general trends. For instance, our results in Fig. 2 showed that compounds containing Fe^{4+} or Ni^{4+} generally exhibit poor thermal stability, which can be easily understood: the nonbonding t_{2g} orbitals of Fe^{4+} and Ni^{4+} are so low in energy (corresponding to high redox potentials in Fig. 8a) that fluorine 2p bands begin to participate in the oxidation process, resulting in the fluorine gas releasing. This coincidence between calculations and physical intuition gave us confidence in the validity of our predictions.

Besides thermal stability, chemical decomposition of compounds under the air environment is another safety issue. Based on the consideration that bond dissociation energies (under ambient conditions) of M-F bonds (M stands for metals considered in this work) are generally larger than those of M-O bonds (e.g., 423 kJ/mol for Mn-F *vs.* 402 kJ/mol for Mn-O, 435 kJ/mol for Ni-F *vs.* 391.6 kJ/mol for Ni-O),[6] we believed that compounds included in this work should be chemical stable under air environments, at least when temperature is not too high. As shown in a recent work,[7] researchers showed that the Na_2MnVF_7 compound did not decompose until the temperature reached 350 ℃, which is far beyond the upper limit of the typical operating temperature of cells.

(IV) Pseudo-binary phase diagrams for compounds with high energy density

Our screening procedure returned a total of 10 compounds. Figure S3 shows their pseudo-binary phase diagrams between charged and discharged end members. Note that there may be different redox reaction pathways for different systems (see x axis of each panel in Fig. S3). For instance, Na_2MnVF_7 compound should be electrochemically cycled between $MnVF_7$ and Na_2MnVF_7 end members, but Na_2MnNiF_7 should be cycled between $NaMnNiF_7$ and Na_3MnNiF_7 end members instead.
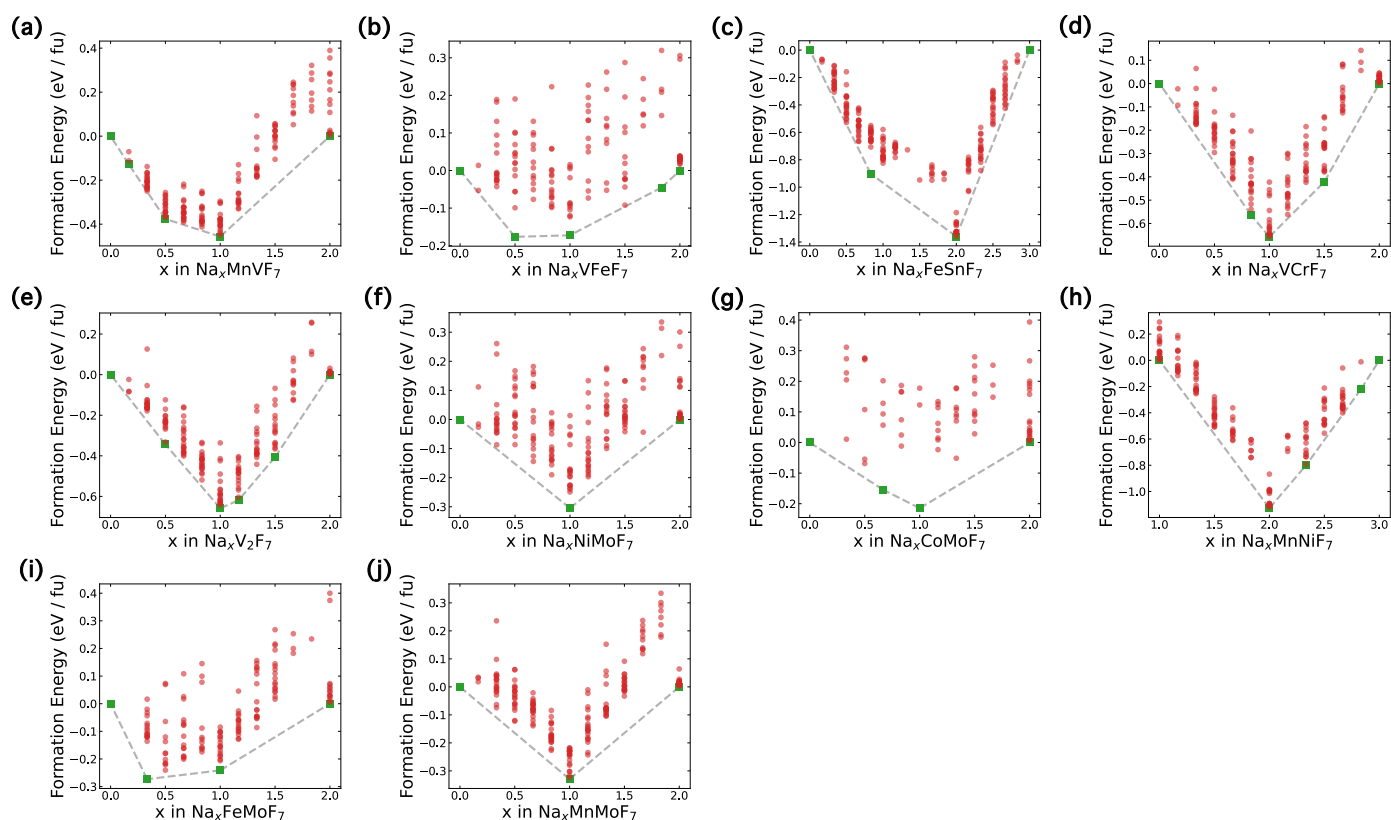
Figure S3. Pseudo-binary phase diagrams for screened compounds with high energy density. For different chemical systems, there may be different redox reaction pathways (see x axis of each panel in the figure).

(V) Migration barriers for compounds with high energy density
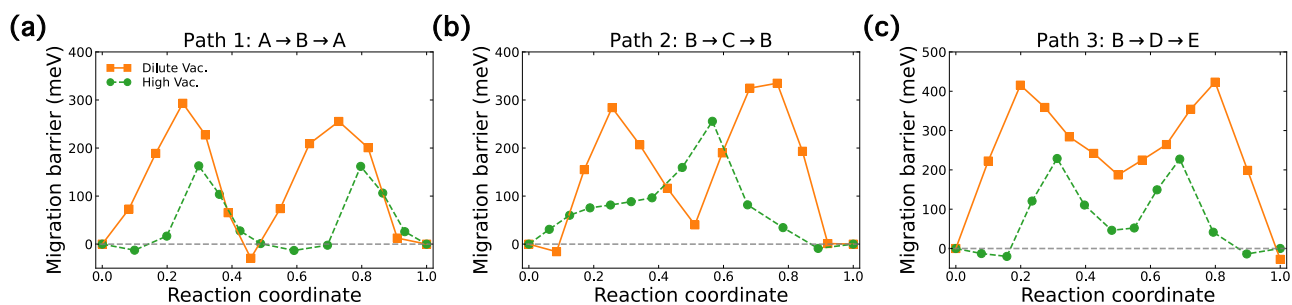
Figure S4. Migration barriers of Na₂MnVF₇ along three paths under dilute and high vacancy limits.
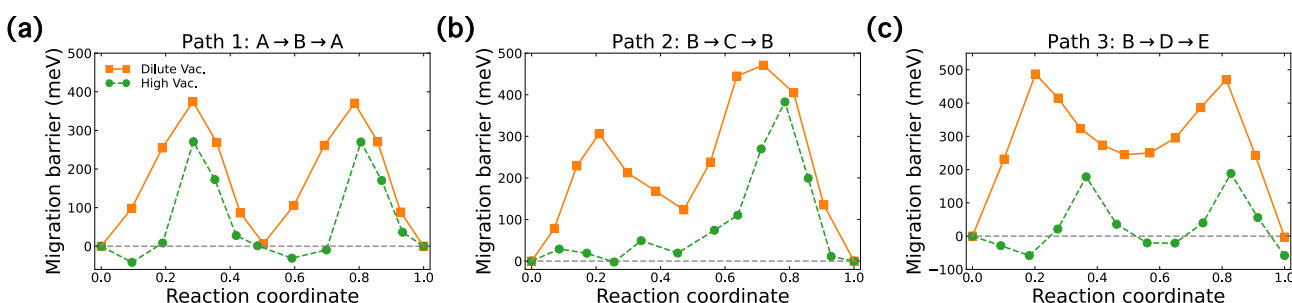
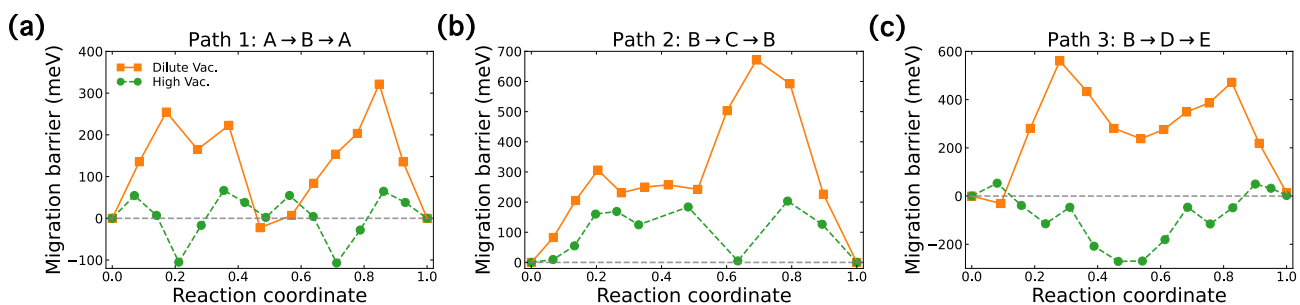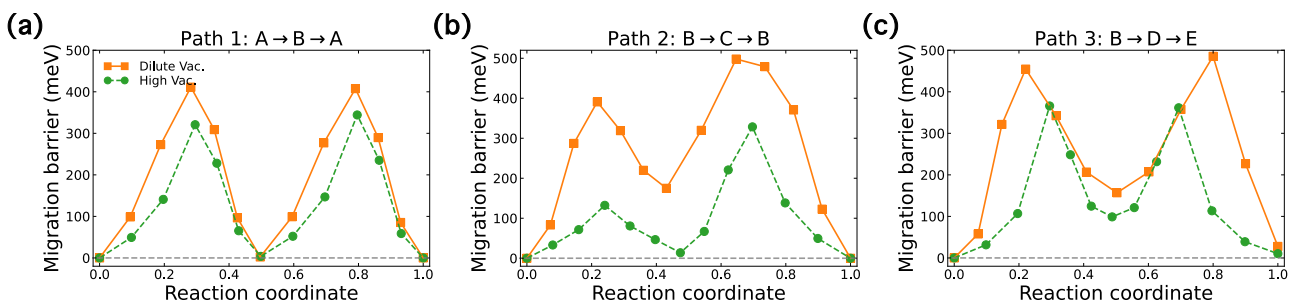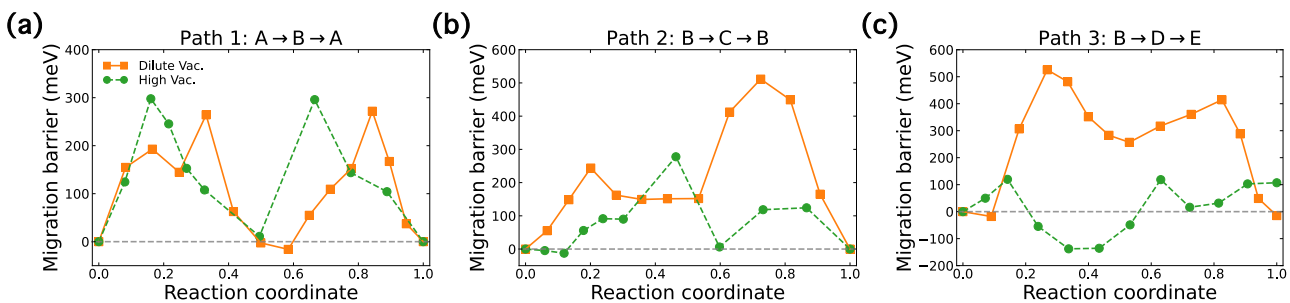**Figure S5. Migration barriers of Na₂VFeF₇ along three paths under dilute and high vacancy limits.**
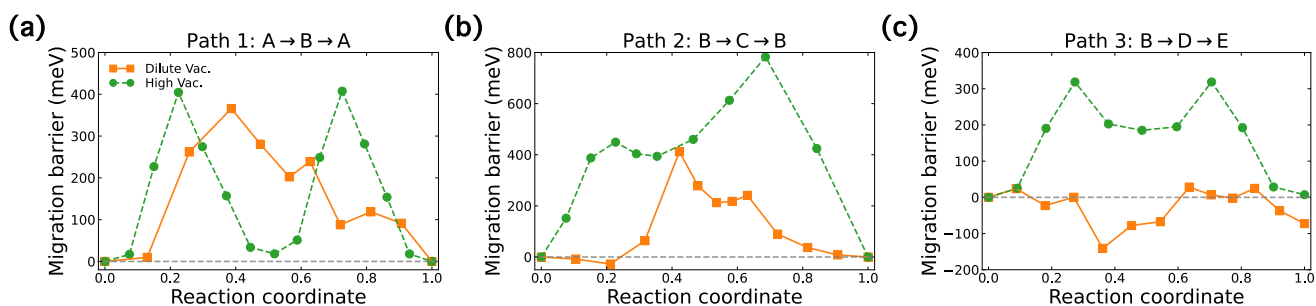
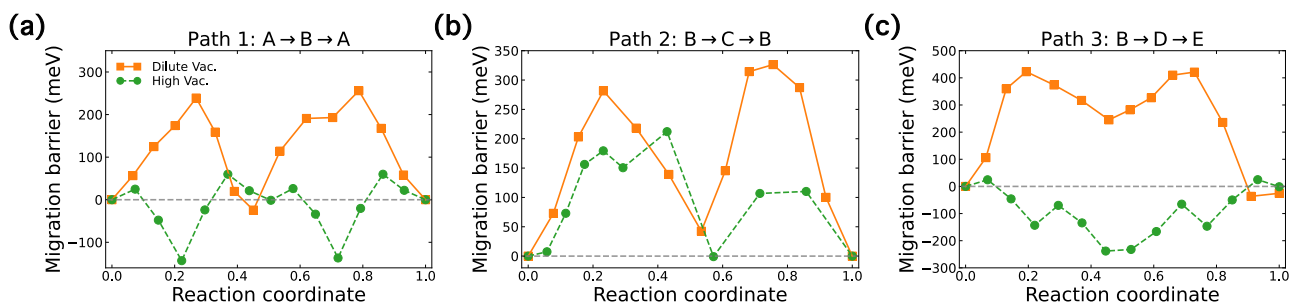**Figure S6. Migration barriers of Na₂FeSnF₇ along three paths under dilute and high vacancy limits.**
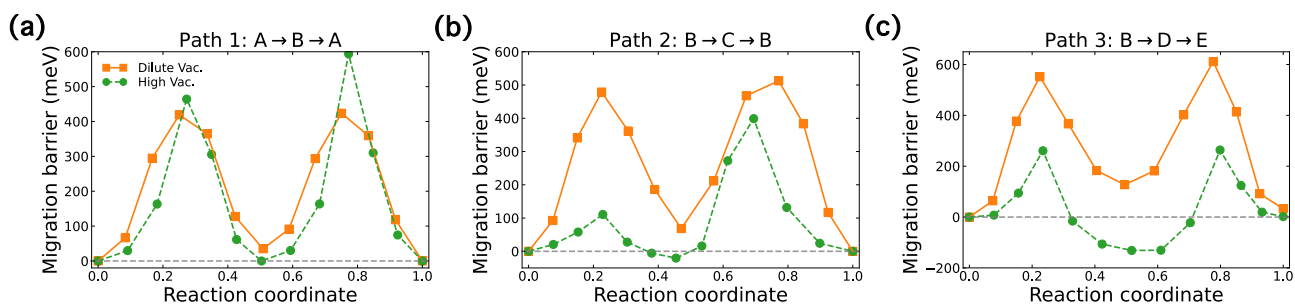
Figure S7. Migration barriers of Na₂VCrF₇ along three paths under dilute and high vacancy limits.
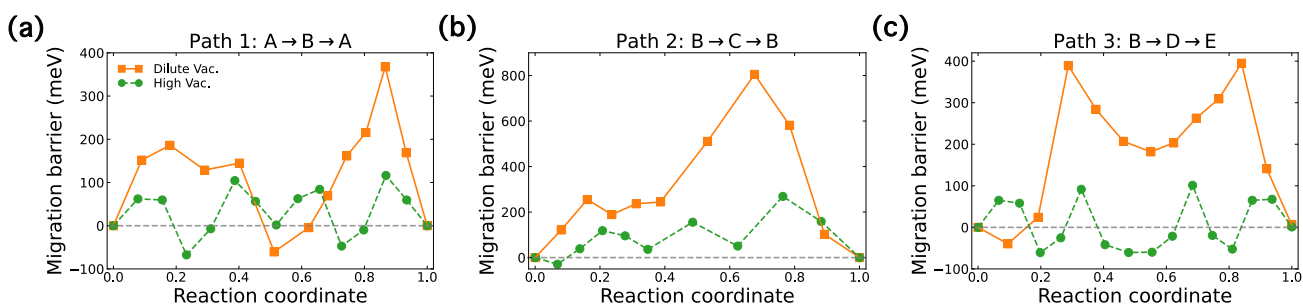
Figure S8. Migration barriers of Na₂NiMoF₇ along three paths under dilute and high vacancy limits.

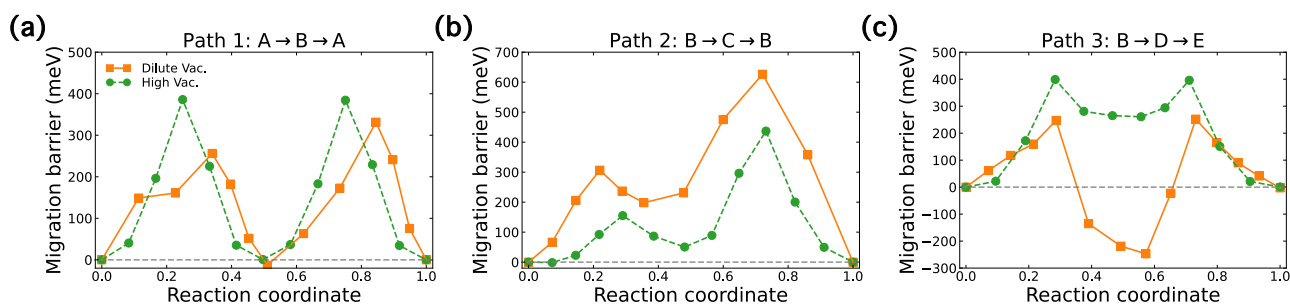**Figure S9. Migration barriers of Na₂CoMoF₇ along three paths under dilute and high vacancy limits.**

Figure S10. Migration barriers of Na₂MnNiF₇ along three paths under dilute and high vacancy limits.

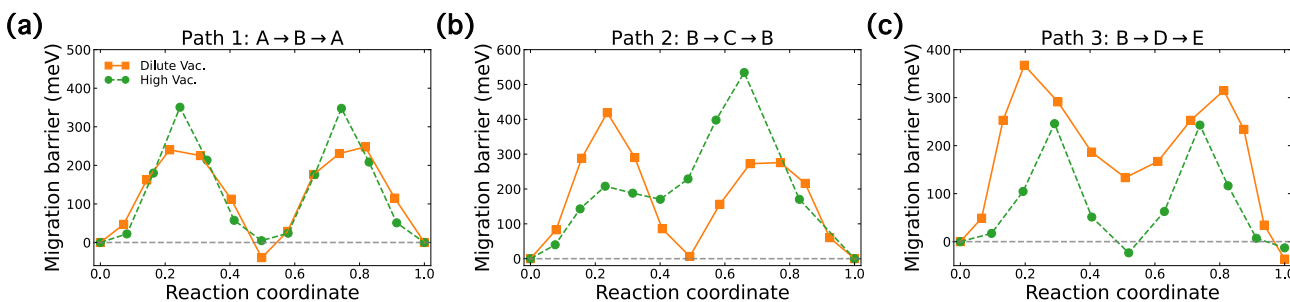**Figure S11. Migration barriers of Na₂FeMoF₇ along three paths under dilute and high vacancy limits.**

(a) Path 1: A → B → A
(b) Path 2: B → C → B
(c) Path 3: B → D → E

Figure S12. Migration barriers of Na$_2$MnMoF$_7$ along three paths under dilute and high vacancy

(a) Path 1: A → B → A
(b) Path 2: B → C → B
(c) Path 3: B → D → E

Figure S13. Migration barriers of Na$_2$TiFeF$_7$ along three paths under dilute and high vacancy limits.

(a) Path 1: A → B → A
(b) Path 2: B → C → B
(c) Path 3: B → D → E

Figure S14. Migration barriers of Na$_2$Fe$_2$F$_7$ along three paths under dilute and high vacancy limits.

(VI) Explanation for 4.7 V equilibrium potential in Na_2MnVF_7 voltage profile

As shown in the Fig. 6a, we predicted an unexpected equilibrium voltage plateau of about 4.7 V for Na_2MnVF_7. This 4.7 V voltage is related to the V^{4+}/V^{5+} redox couple, implying half of the Mn ions in the compound are still in the oxidation state of +2 at the end state of charge. As described in the main text, this is a surprising phenomenon because Mn^{2+} ion should be oxidized preferentially over V^{4+} ion (~4 V redox-potential for Mn^{2+}/Mn^{3+} versus ~4.7 V for V^{4+}/V^{5+}, see Fig. 8a). In the following part of this section, we will explain this phenomenon from a structural point of view.
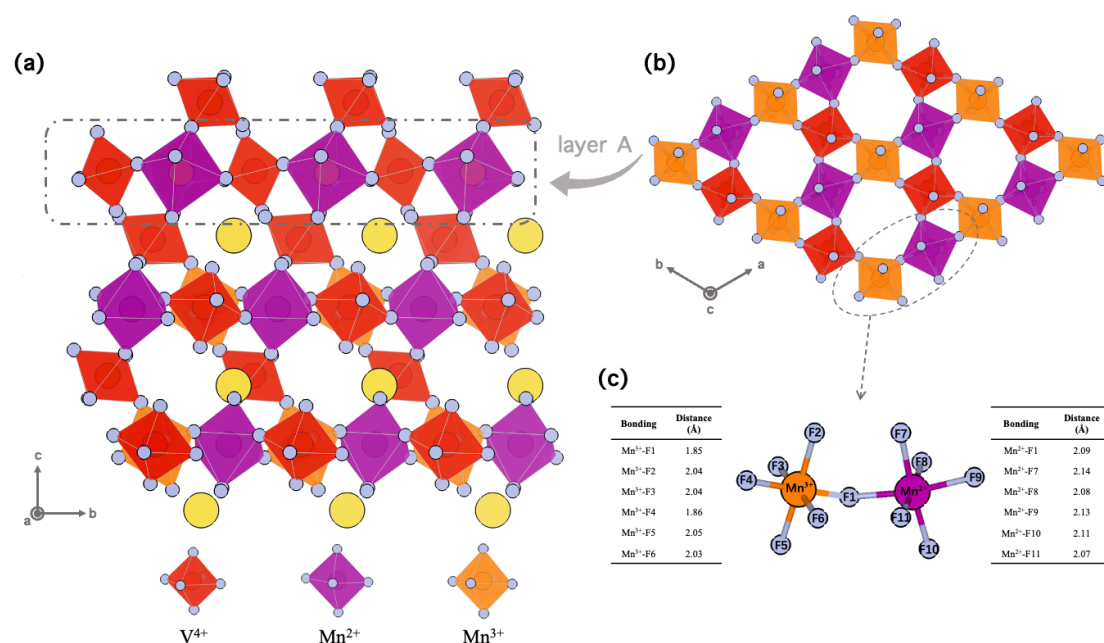
Figure S15. (a) Detailed crystal structure of $Na_{0.5}MnVF_7$ compound, in which V is in the oxidation state of +4 (red), Mn is in the oxidation state of +2 (purple) or +3 (orange). (b) Detailed structure of stacking layer A, viewing along the [001] direction. (c) Bonding distances for $Mn^{3+}F_6$, and $Mn^{2+}F_6$ Octahedrons.

In Fig. S15a, we exhibited the detailed crystal structure of $Na_{0.5}MnVF_7$, which is one of the stable phases in the pseudo-binary $MnVF_7$-Na_2MnVF_7 phase diagram ($Na_{0.5}MnVF_7$ in Fig. S3a). In the $Na_{0.5}MnVF_7$ crystal structure, all of the V ions are in the +4 oxidation state, and half of the Mn ions are in the +3 oxidation state (the rest are in the +2 oxidation state). Normally speaking, as the desodiated process proceeds, the

remaining half of Mn^{2+} should be gradually oxidized to Mn^{3+} until there are only Mn^{3+} ions in the system at the end state of charge. However, as shown in the Fig. S15b, corner-sharing $Mn^{3+}F_6$ and $Mn^{2+}F_6$ octahedrons form an infinity chain along the [100] direction, leading to a strong structural coupling between Mn^{3+} and Mn^{2+} ions. Due to the Jahn-Teller effect, prominent structural distortions are expected to occur in $Mn^{3+}F_6$ octahedrons. Indeed, as shown in Fig. S15c, two of the six Mn^{3+}-F bonds (Mn^{3+}-F1 and Mn^{3+}-F4) dramatically shrink. As a result, this structural distortion will make electron cloud of F^- closer to Mn^{3+} ions, which equivalently means that the electron cloud of F^- will be far away from Mn^{2+} ions. According to the crystal filed theory, the energy of the antibonding e_g orbitals of Mn^{2+} (we don't consider possible orbital splitting for e_g here) should decline. With a relatively small energy difference between V^{4+}/V^{5+} and Mn^{2+}/Mn^{3+} orbitals, this energy decreases for Mn^{2+} orbitals may lead to an early activation of the nonbonding t_{2g} orbitals of V^{4+}. We drew a schematic diagram to illustrate this phenomenon, shown in Fig. S16a. A two-dimensional slice of the charge density of $Na_{0.5}MnVF_7$ (along [001] direction) is displayed in Fig. S16b. From the contours of charge density, it is obvious that the electron cloud of F^- is closer to Mn^{3+} than Mn^{2+}, which further improve our arguments.
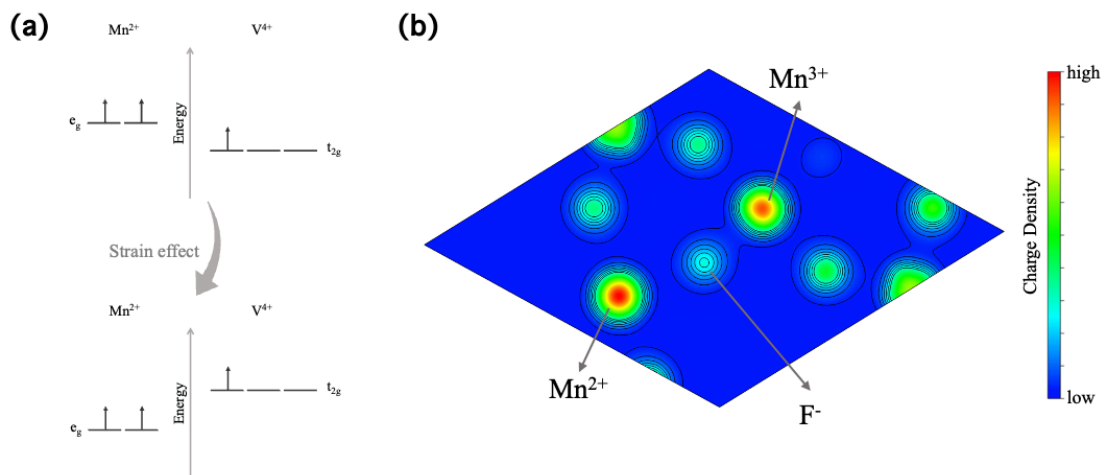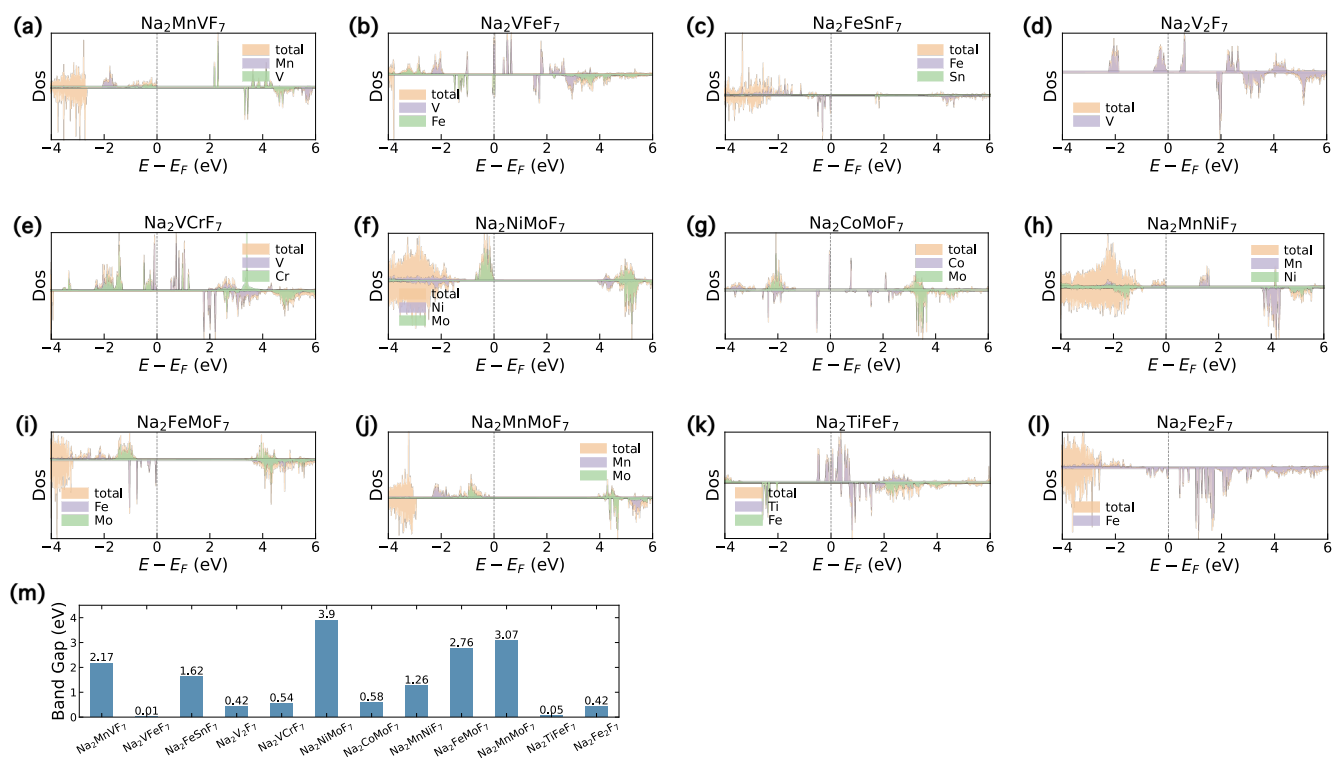

Figure S16. (a) A schematic diagram describing how the Jahn-Teller effect of Mn^{3+} affects the e_g orbitals of Mn^{2+}. (b) A two-dimensional slice of the charge density of $NaMn_2V_2F_{12}$.

(VII) Evaluation of electronic conduction for T-Na₂MM'F₇ compounds

Figure S17. Density of states for (a) Na2MnV₇, (b) Na₂VFeF₇, (c) Na₂FeSnF₇, (d) Na₂V2F₇, (e) Na₂VCrF₇, (f) Na₂NiMoF₇, (g) Na₂CoMoF₇, (h) Na₂MnNiF₇, (i) Na₂FeMoF₇, (j) Na₂MnMoF₇, (k) Na₂TiFeF₇, and (l) Na₂Fe₂F₇. (m) A band-gap histogram.
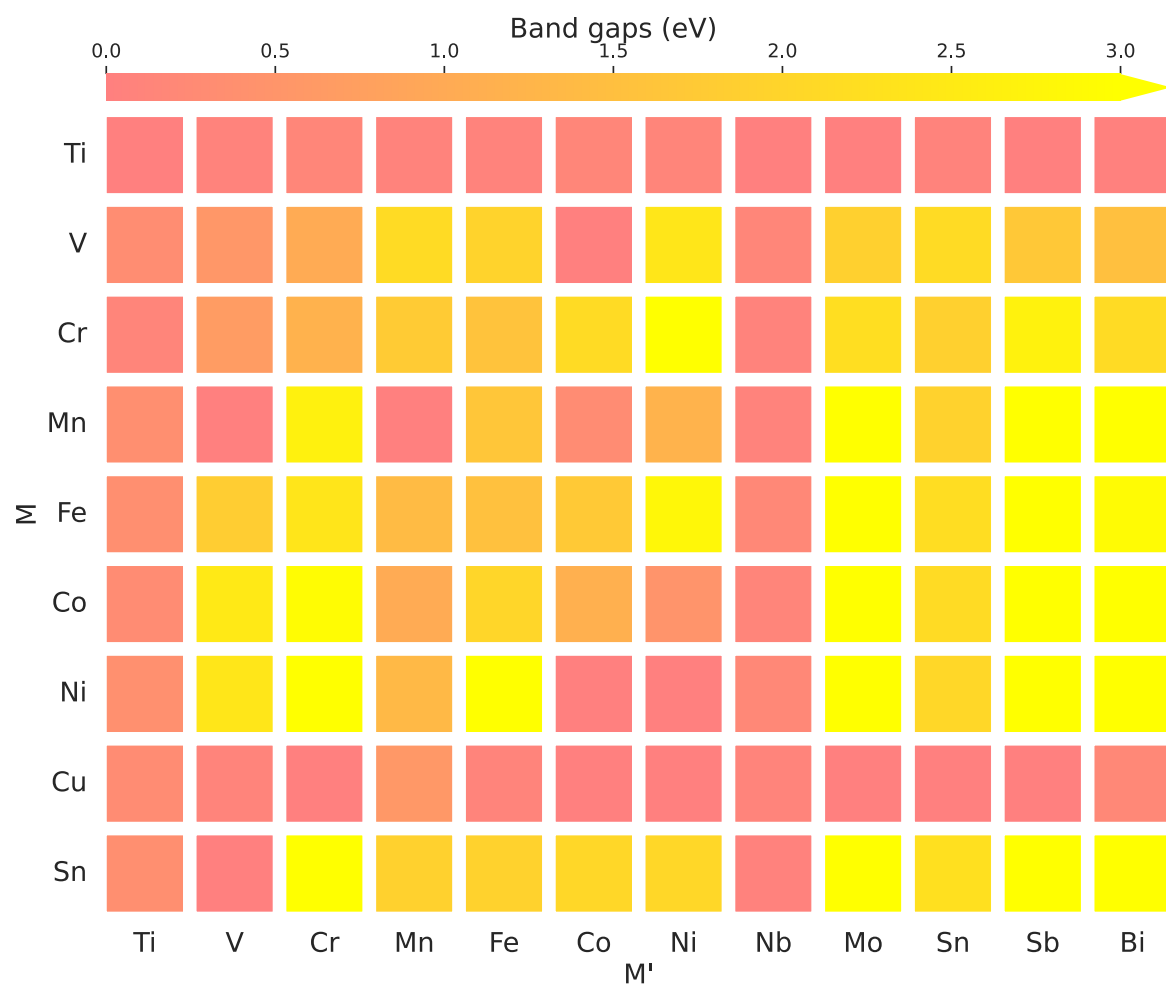
Figure S18. A heatmap of band gaps.

(VIII) Quantitative electrochemical metrics of all the weberite-type compounds evaluated in this work

Table S3. The quantitative electrochemical metrics of all weberite-type compounds depicted in Fig. 3a. It should be noted that this table only contains compounds that demonstrate moderate-to-high thermodynamic stability ($E_{hull} < 100$ meV/atom).

Formula	Cycling range	Average voltage (V)	Gravimetric capacity (mAh/g)	Specific energy (Wh/kg)
Na2MnVF7	0-2	3.99	199	795
Na2FeVF7	0-2	3.65	199	727
Na2SnFeF7	0-3	2.86	228	652
Na2CrVF7	0-2	3.19	202	645
Na2V2F7	0-2	3.16	204	646
Na2NiMoF7	0-2	3.69	166	615
Na2CoMoF7	0-2	3.63	168	609
Na2NiMnF7	1-3	3.41	178	609
Na2FeMoF7	0-2	3.54	169	600
Na2MnMoF7	0-2	3.52	168	595
Na2CoFeF7	1-3	3.35	176	590
Na2Sn2F7	0-3	2.98	193	575
Na2FeSbF7	0-2	3.64	156	568
Na2Mn2F7	1-3	3.14	179	562
Na2FeTiF7	0-2	2.83	202	575
Na2MnFeF7	1-3	3.02	178	537
Na2CrMoF7	0-2	3.07	170	522
Na2NiSbF7	0-2	3.48	149	519
Na2VMoF7	0-2	3.04	171	519
Na2CrSbF7	0-2	3.29	157	517
Na2CoSbF7	0-2	3.42	149	510
Na2VSnF7	0-2	3.19	159	507
Na2MnSbF7	0-2	3.33	151	503
Na2CrSnF7	0-2	3.22	153	492
Na2SnMoF7	0-2	3.44	140	482
Na2CrTiF7	0-2	2.31	201	464
Na2Fe2F7	1-3	2.57	181	467
Na2VTiF7	0-2	2.25	202	455
Na2SnSbF7	0-2	3.20	132	423
Na2MnCrF7	1-2	4.46	94	419
Na2SnBiF7	0-2	3.29	108	355
Na2FeCrF7	1-2	3.68	93	342
Na2NiVF7	1-2	3.60	93	335
Na2CoVF7	1-2	3.55	93	330

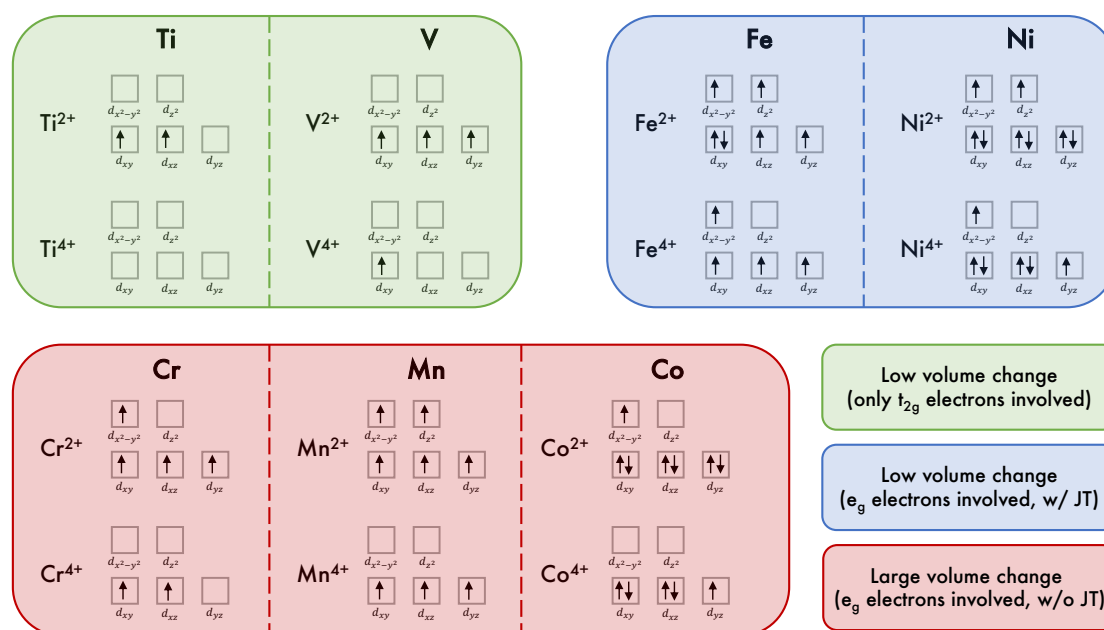|				
Na2Ni2F7	2-3	3.69	84	310
Na2VNbF7	0-2	1.74	172	299
Na2CrNbF7	0-2	1.72	172	296
Na2MnNbF7	0-2	1.73	170	294
Na2CuCoF7	2-3	3.29	83	273
Na2CoNiF7	2-3	3.12	84	262
Na2Cr2F7	1-2	2.69	95	256
Na2MnBiF7	1-2	4.00	61	244
Na2Co2F7	2-3	2.71	84	228
Na2Ti2F7	0-1	2.12	106	225
Na2MnCoF7	2-3	2.65	85	225
Na2FeBiF7	1-2	3.43	60	206
Na2NiTiF7	1-2	1.83	94	172
Na2MnTiF7	1-2	1.60	95	152
Na2VBiF7	1-2	2.39	61	146
Na2FeNiF7	2-3	1.69	85	144
Na2CrBiF7	1-2	2.36	61	144

(IX) Volume changes of weberite compounds upon cycling

Table S4. Detailed volume changes of weberite $Na_2M_2F_7$ compounds upon cycling.

Formula	Volume change (with respect to the volume of the $Na_2M_2F_7$)		
	$Na_2M_2F_7$	$Na_1M_2F_7$	$Na_0M_2F_7$
Na2Ti2F7	0%	-3.1%	2.8%
Na2V2F7	0%	0.5%	6%
Na2Cr2F7	0%	4.8%	11%
Na2Mn2F7	0%	4.6%	12.2%
Na2Fe2F7	0%	0.6%	6.3%
Na2Co2F7	0%	2.7%	9.4%
Na2Ni2F7	0%	1.6%	7%

Figure S19. Distribution of *d*-orbital electrons for 3d transition metals under different oxidation states.

Supporting References

[1] H. Park, Y. Lee, M.-k. Cho, J. Kang, W. Ko, Y.H. Jung, T.-Y. Jeon, J. Hong, H. Kim, S.-T. Myung, J. Kim, Na2Fe2F7: a fluoride-based cathode for high power and long life Na-ion batteries, Energy & Environmental Science, 14 (2021) 1469-1479.

[2] J. Kang, J. Ahn, H. Park, W. Ko, Y. Lee, S. Lee, S. Lee, S.K. Jung, J. Kim, Highly

Stable Fe2+/Ti3+‐Based Fluoride Cathode Enabling Low‐Cost and High‐Performance

Na‐Ion Batteries, Advanced Functional Materials, (2022).

[3] S.P. Ong, L. Wang, B. Kang, G. Ceder, Li−Fe−P−O2 Phase Diagram from First Principles Calculations, Chemistry of Materials, 20 (2008) 1798-1807.

[4] S.P. Ong, A. Jain, G. Hautier, B. Kang, G. Ceder, Thermal stabilities of delithiated olivine MPO4 (M=Fe, Mn) cathodes investigated using first principles calculations, Electrochemistry Communications, 12 (2010) 427-430.

[5] M.W. Chase, N.I.S. Organization, NIST-JANAF thermochemical tables, American Chemical Society Washington, DC, 1998.

[6] J. Speight, Lange's handbook of chemistry, McGraw-Hill Education, 2005.

[7] J. Liao, J. Han, J. Xu, Y. Du, Y. Sun, L. Duan, X. Zhou, Scalable synthesis of Na2MVF7 (M = Mn, Fe, and Co) as high-performance cathode materials for sodium-ion batteries, Chemical Communications, 57 (2021) 11497-11500.

[8] R.E. Doe, K.A. Persson, Y.S. Meng, G. Ceder, First-Principles Investigation of the Li−Fe−F Phase Diagram and Equilibrium and Nonequilibrium Conversion Reactions of Iron Fluorides with Lithium, Chemistry of Materials, 20 (2008) 5274-5283.